

Highlights

SGEMM-cube: Emulating FP32 GEMM on Ascend NPUs using FP16 Cube Units with Precision Recovery

Weicheng Xue, Baisong Xu, Kai Yang, Yongxiang Liu, Dengdeng Fan, Pengxiang Xu, Yonghong Tian

- Emulate FP32 GEMM using FP16-only matrix engines with high precision
- Tunable scaling and decomposition strategy to preserve up to 22-bit mantissa
- termwise accumulation improves numerical stability in low-exponent regimes
- Cache-aware blocking and pipelining achieves 77% of peak performance

SGEMM-cube: Emulating FP32 GEMM on Ascend NPU using FP16 Cube Units with Precision Recovery

Weicheng Xue^{a,1}, Baisong Xu^{a,1}, Kai Yang^{a,1}, Yongxiang Liu^a, Dengdeng Fan^a, Pengxiang Xu^{a,*}, Yonghong Tian^{a,*}

^a*Pengcheng Laboratory, 6001 Shahe West Road, Shibilong, Shenzhen, 518055, Guangdong, China*

Abstract

Low-precision matrix engines, such as FP16 cube, offer high throughput but lack support for full-precision computation. In this work, we propose SGEMM-cube, a high-performance algorithm for emulating FP32 general matrix-matrix multiplication (GEMM) using only FP16 computation units on a representative AI accelerator. The method decomposes each FP32 operand into two FP16 values and compensates for numerical errors through a tunable scaling strategy. A detailed analysis of numerical errors, including underflow conditions and precision loss, guides the selection of scaling parameters to preserve up to 22 bits of mantissa accuracy. We further investigate the effect of computation order on accuracy and demonstrate that a termwise accumulation scheme improves numerical stability over conventional FP32 GEMM in low-exponent regimes. Finally, a cache-aware blocking strategy and double-buffered pipeline are introduced to overlap memory transfers with computation, enabling SGEMM-cube to achieve up to 77% of the theoretical FP32-equivalent peak performance on Ascend 910A NPU lacking native FP32 support. Extensive numerical experiments confirm that our method not only recovers the accuracy of native FP32 GEMM but also exhibits superior numerical stability under certain conditions, due to its structured and error-aware computation order.

Keywords: FP32 emulation, FP16 cube, numerical stability, matrix decomposition, high-performance computing, mixed precision

*Corresponding authors: Pengxiang Xu (xupx@pcl.ac.cn), Yonghong Tian (tianyh@pcl.ac.cn).

¹These authors contributed equally to this work.

1. Introduction

The evolution of specialized accelerators is reshaping the landscape of high-performance computing (HPC). Driven by the rapid progress in deep learning, modern computer systems increasingly rely on heterogeneous architectures that integrate domain-specific hardware. Processors such as NVIDIA GPUs with Tensor Cores, Google’s TPUs, and emerging Neural Processing Units (NPUs) deliver significant speedups for matrix-dominated workloads, offering orders of magnitude higher throughput than traditional CPUs.

These accelerators achieve high performance by concentrating their compute resources on low-precision formats such as half-precision floating point (FP16), bfloat16 (BF16), and INT8. While these formats are sufficient for many machine learning tasks, they are often inadequate for deep learning, scientific and engineering applications [1, 2, 3, 4, 5, 6], which demand the accuracy and dynamic range of FP32 or FP64 arithmetic. This mismatch presents a growing challenge: the most powerful computing platforms are optimized for formats that are incompatible with the precision requirements of many established scientific workloads.

To bridge this gap, this work investigates how to efficiently harness the compute density of low-precision hardware for workloads that require FP32-level accuracy. Specifically, we target scenarios where native FP32 matrix multiplication (GEMM) is unsupported or inefficient, such as on Ascend 910A NPUs that expose high-performance FP16 tensor engines but lack equivalent FP32 compute units.

We propose **SGEMM-cube**, a software–hardware co-designed framework that enables high-throughput and high-accuracy FP32 GEMM using only FP16 computation. At its core, SGEMM-cube combines a numerical emulation technique with a performance-optimized implementation tailored to the memory hierarchy of a representative AI accelerator.

The main contributions of this work are:

- **A robust algorithm for FP32 emulation:** We present SGEMM-cube, an algorithm that decomposes each FP32 operand into a pair of FP16 values, a high-order component and a residual, and recombines their products to reconstruct FP32-level results, preserving up to 22 bits of mantissa accuracy.

- **Comprehensive error analysis and numerical control:** We perform a detailed study of precision loss due to rounding and underflow, and introduce two mitigation strategies: (1) a tunable amplification factor applied to residual terms, and (2) a termwise accumulation scheme that improves numerical stability over traditional reduction orders.
- **Architecture-aware optimization:** We develop a set of performance strategies including L1-cache-aware tiling and a software-level double-buffered pipeline. These techniques overlap memory movement and computation, effectively hiding data transfer latency and enabling high hardware utilization.
- **Empirical validation:** We rigorously evaluate SGEMM-cube on Ascend 910A, a representative AI accelerator with FP16-only GEMM engines. Results show that SGEMM-cube achieves up to 77% of the FP32-equivalent theoretical peak and, in some cases (e.g., low-exponent inputs), exhibits superior numerical stability due to its structured and error-aware computation order.

2. Background and Related Work

The increasing divergence between the numerical precision demands of scientific computing and the capabilities of modern AI-oriented accelerators (seen in Table 1) has spurred significant research into mixed-precision algorithms [7, 8, 9, 10]. While many scientific applications still demand FP32 or FP64 precision for numerical stability, contemporary hardware increasingly favors lower-precision formats such as FP16 or even FP8 to maximize throughput and energy efficiency. For example, the FP8 Tensor Core throughput of the NVIDIA H100 is roughly $60\times$ higher than its FP64 throughput, and the Ascend 910A NPU [11] delivers ~ 256 TF/s in FP16 but lacks efficient support for FP32 GEMM. These trends underscore a critical question: *how to emulate high-precision matrix computations using low-precision arithmetic units without compromising accuracy?*

A conventional approach to address the precision–performance tradeoff is through mixed-precision techniques [7, 8, 9, 10]. The idea of performing most computations in lower precision and then refining results in higher precision has a long history in numerical linear algebra, particularly in iterative refinement solvers. These methods rely on selectively using high-precision

Table 1: TFlops of typical AI chips

Chip Model	FP16	FP32	FP64
Nvidia H100 SXM	989	67	34
Nvidia A100 SXM	312	19.5	9.7
AMD MI300X	1307	163	81
Intel Gaudi3	1678	14.3	-
Huawei Ascend 910A	256	-	-
Cambricon MLU370-X8	96	24	-
Baidu Kunlun XPU-R	400	-	-
Muxi Xiyun C500	280	36	-
Shenwei SW26010-Pro	55.3	-	13.8
Moore Threads MTT S4000	100	25	-

arithmetic in numerically sensitive operations, while exploiting faster low-precision operations elsewhere to gain performance.

In contrast to such hybrid strategies, recent work has explored a more direct approach: emulating high-precision GEMM (e.g., FP32) using only low-precision hardware such as FP16. Rather than mixing precisions, these methods decompose each high-precision operand into two or more low-precision components, typically capturing the high and low bits of the significand, and reformulate the original matrix product as a sum of multiple low-precision GEMMs. This line of work aims to preserve high numerical accuracy while operating entirely on accelerators that lack efficient FP32 units.

The foundational work by Ozaki et al. [12] formalized this idea by expressing the product of two FP64 matrices as a series of lower-precision GEMMs with a priori error bounds. Although originally targeted at double precision, this decomposition strategy laid the groundwork for FP32-from-FP16 emulation schemes. Markidis et al. [13] were among the first to explore such techniques on GPUs, proposing a two-pass approach based on splitting FP32 inputs into FP16 components. Their method performed an initial FP16 GEMM followed by a corrective residual GEMM. However, their use of round-towards-zero (RZ) conversion introduced a systematic 2-bit precision loss compared to full FP32 accuracy, owing to uncorrected rounding errors in the low-order bits.

To reduce this error, Feng et al. [14] proposed Egemm-TC, a refinement that adopted a more careful decomposition and a rounding strategy closer to round-to-nearest (RN). Their implementation included warp-level cache reuse and register pipeline optimizations, yielding a $3.13\times$ speedup over cuBLAS

FP32 GEMM on NVIDIA Turing GPUs. However, the decomposition still failed to fully account for the implicit leading bit in FP32 representation, limiting the worst-case precision to approximately 21 bits.

Ootomo and Yokota [15] later identified another key source of error: the use of Tensor Cores for accumulation. Tensor Core units perform multiplications in FP16 but may accumulate results using internal FP32 registers with RZ rounding [16]. This caused a systematic bias that could not be corrected by earlier schemes. They proposed performing the residual accumulation outside the Tensor Core, using standard FP32 units with unbiased RN rounding. By scaling intermediate terms to prevent underflow and carefully structuring the summation, their approach achieved bit-for-bit FP32 accuracy on A100 GPUs. Performance-wise, their CUTLASS-based implementation delivered up to 51 TFLOPS, more than $2\times$ the peak native FP32 throughput. To support matrices spanning the full FP32 exponent range, they later integrated TensorFloat-32 (TF32) into their framework, attaining ~ 33 TFLOPS with negligible (~ 1 -bit) precision loss.

Ma et al. [17] further advanced this field by introducing an optimized operand decomposition scheme that emulates FP32 precision using only FP16 operations. Their method carefully accounts for the implicit leading bit in the FP32 mantissa, reducing the worst-case error to approximately one bit. To sustain high throughput, they implemented different memory pipeline strategies that overlaps tile loading with computation, ensuring that the Tensor Cores remain fully utilized. Their implementation on NVIDIA A100 achieved 64.15 TFLOPS FP32-equivalent GEMM, approximately 61.7% of the chip’s theoretical FP16 peak, while preserving near-full FP32 accuracy.

In parallel to these FP32-from-FP16 emulation schemes, Li et al. [18] proposed QuanTensor, a general low-precision tensor computation framework for GPUs. QuanTensor decomposes high-precision GEMMs into multiple low-precision GEMMs combined with residual correction to recover accuracy. By flexibly choosing the low-precision type and number of passes, it enables a tunable trade-off between throughput and precision. On NVIDIA GPUs, the INT8 variant achieves the highest throughput, while FP16/BF16 variants offer better numerical stability with moderate performance gains. However, its multi-pass design requires repeated quantization and dequantization on the GPU platform, which can incur non-trivial overhead when many passes are used or when high accuracy is required.

A summary of related works is given in Table 2. Despite these advances, challenges remain. A single FP16 multiplication carries at most ~ 11 bits of

precision (including the hidden bit), compared to 24 bits in FP32. Therefore, converting and computing in FP16 inevitably introduces quantization and accumulation errors. Two-pass methods recover much of the lost accuracy, but small residual errors persist unless additional corrective passes are introduced. Accumulating many FP16 products is also nontrivial due to the narrow exponent range of FP16, which can lead to overflow, underflow or cancellation errors. Algorithms must carefully structure their summations, by summing larger terms first or splitting into multiple passes, to preserve numerical significance.

To make such error-reduction techniques practical without sacrificing performance, it is essential to minimize their computational and memory overhead. The most effective methods address this by incorporating system-level optimizations, including tiling and cache-aware buffering strategies, which help hide memory latency and keep low-precision units fully utilized. In this context, we propose **SGEMM-cube**, a novel algorithm for single-precision GEMM emulation on hardware with only FP16 matrix engines. SGEMM-cube is designed to combine high numerical accuracy with high sustained throughput on accelerators that lack efficient FP32 support. Its key innovation lies in its unified design: it integrates a numerically accurate decomposition scheme with a system-level pipelining strategy to minimize memory overhead and maximize hardware utilization.

Numerically, SGEMM-cube splits each FP32 matrix into two FP16 components and performs multiple scaled GEMMs whose products are termwise accumulated. This strategy is shown to achieve FP32 accuracy and, in some cases, surpass it. On the system side, SGEMM-cube employs cache-aware tiling and double buffering to overlap data movement with computation. Tiles are sized to fit in L1 buffer, and two streams of tiles are maintained in alternating buffers to hide load/store latency. As a result, the additional computation introduced by decomposition does not stall the pipeline, ensuring that the FP16 units remain fully utilized.

3. Methodology

3.1. Floating-Point Decomposition Algorithm

3.1.1. Fundamentals of FP32 to FP16 Decomposition

According to the IEEE-754 floating-point standard [19], a single-precision (FP32) number is represented using 32 bits: 1 sign bit (S), 8 exponent bits

Table 2: Comparison of FP32 emulation methods using FP16 hardware

Work	Hardware Target	Decomposition / Rounding Method	Precision Loss	Error Control Mechanisms	Performance Claim
Markidis et al. [13]	NVIDIA V100	Truncation-based (RZ)	2 bits	Not detailed	Trade-off between performance and precision
Feng et al. [14]	NVIDIA T4 & RTX6000	Decomposition without hidden bit, RZ	2 bits	Warp-level cache/register pipeline optimization	3.13× speedup over cuBLAS FP32
Ootomo et al. [15]	NVIDIA A100	Decomposition with amplification, RN	1 bit	Lacked detailed underflow/rounding error control	51 TFLOPS (surpassing theoretical FP32 peak)
Ma et al. [17]	NVIDIA V100, T4, A100	Optimized decomposition, RN	1 bit	Lacked deep error control design and analysis	64.15 TFLOPS (61.7% of theoretical peak)
Li et al. [18]	NVIDIA T4, RTX2080Ti	Multi-pass low-precision GEMM (FP16/INT8/INT4) with residual correction	N/A	Configurable & Flexible decomposition	Tunable precision–performance trade-off
This Work (SGEMM-cube)	Ascend 910A	Decomposition with tunable amplification, RN	~1 bit	Tunable amplification, termwise accumulation	65.3 TFLOPS (77% of theoretical FP32-equivalent peak)

(E), and 23 mantissa (fraction) bits (M), with an implicit leading bit for normalized values. The actual value V is given by Eq. 1:

$$V = (-1)^S \times 2^{(E-127)} \times (1.M) \quad (1)$$

Here, $E - 127$ is the offset exponent, and M is a 23-bit fraction. For normalized numbers, the leading bit before the decimal point is implicitly assumed to be 1.

A half-precision (FP16) number uses 16 bits: 1 sign bit, 5 exponent bits, and 10 mantissa (fraction) bits, also with an implicit leading bit. To emulate FP32 precision using FP16 units, an FP32 value V is decomposed into a high-order part (V_{high}) and a low-order residual part (V_{low}), as conceptually illustrated in Fig. 1. This decomposition follows the round-to-nearest-even (RN) rule, which is critical for minimizing rounding errors.

The high part, V_{high} , is derived from the leading 10 bits of the FP32 mantissa together with the implicit leading bit, with the 11th bit used for rounding. In most cases, this rounding bit becomes zero after rounding. A specific edge case arises when the last bit of the high mantissa is zero, the rounding bit is one, and all subsequent bits are zero; in this scenario, the rounding bit is not directly retained in the low part. For the low part, V_{low} ,

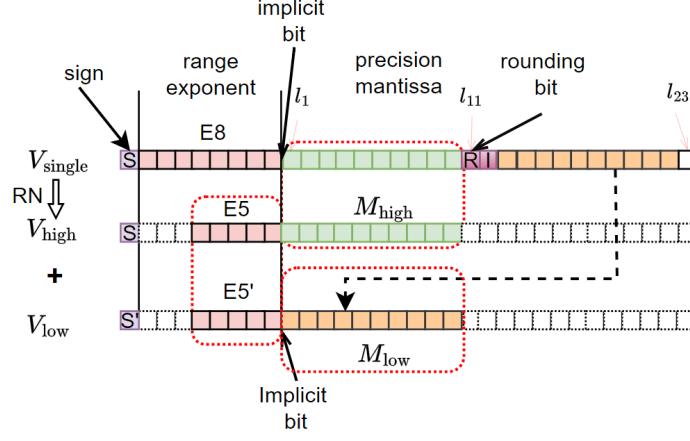


Figure 1: Splitting a single FP32 floating number into two FP16 floating numbers

the remaining 13 bits after rounding are used, starting from the first non-zero bit, and are also rounded according to the RN rule. The decomposition process is formally expressed in Eq. 2:

$$\begin{cases}
 V_{\text{high}} = \begin{cases} (-1)^S \times 2^{(E'-15)} \times 1.M_{\text{high}} & \text{if } 1 \leq E' \leq 30 \text{ (normalized)} \\
 (-1)^S \times 2^{-14} \times 0.M_{\text{high}} & \text{if } E' = 0 \text{ (subnormal)} \end{cases} \\
 V_{\text{low}} = \begin{cases} (-1)^{S'} \times 2^{(E'-15-11-1-N)} \times 1.M_{\text{low}} & \text{if } 1 \leq (E' - 11 - 1 - N) \leq 30 \\
 \text{(normalized)} \\
 (-1)^{S'} \times 2^{-14} \times 0.M_{\text{low}} & \text{if } (E' - 11 - 1 - N) = 0 \\
 \text{(subnormal)} \end{cases}
 \end{cases} \quad (2)$$

Here, E' is the 5-bit FP16 exponent, and $E' - 15$ and $E' - 12 - N - 15$ represent the offset exponents of the high and low parts. R denotes the carry introduced by rounding the high part: $E - 127 + R = E' - 15$, with $R = 1$ if rounding carries, otherwise 0. If $R = 1$, the low part's sign bit may flip. M_{high} and M_{low} are the 11-bit mantissas of the high and low parts, respectively. N is the number of leading zeros in the mantissa of V_{low} after truncation, with $0 \leq N \leq 10$.

The original FP32 value can be approximately reconstructed by summing the two FP16 components: $V \approx V_{\text{high}} + V_{\text{low}}$. This decomposition theoretically preserves at least 22 mantissa bits, one less than FP32 and 11 more than a standalone FP16 representation, thereby enabling significant accu-

racy recovery. While it introduces additional computational cost and hardware/software support requirements, it enhances flexibility under hardware precision constraints, usually exist for modern AI chips.

3.1.2. Probability of Underflow and Gradual Underflow

Underflow and gradual underflow are critical numerical phenomena that primarily affect the low-order component, V_{low} , due to its smaller magnitude. Given Ascend processors adopt RN rounding, we analyze the probabilities of these events accordingly. Let $P(N = n, X)$ be the probability of an event X (truncation T or rounding R) given $N = n$:

$$P(N = n, X) = \begin{cases} 0 & \text{if } n < -1 \\ \left(\frac{1}{2}\right)^{l_M - l_{M_{\text{high}}} + 1} & \text{if } n = -1 \text{ and } X = T \text{ or } R \\ \left(\frac{1}{2}\right)^{n+2} & \text{if } 0 \leq n < l_M - l_{M_{\text{high}}} - 1 \text{ and } X = T \text{ or } R \\ \left(\frac{1}{2}\right)^{l_M - l_{M_{\text{high}}}} & \text{if } n = l_M - l_{M_{\text{high}}} - 1 \text{ and } X = T \\ 0 & \text{if } n = l_M - l_{M_{\text{high}}} - 1 \text{ and } X = R \end{cases} \quad (3)$$

Here, $l_M = 23$ (FP32 mantissa), and $l_{M_{\text{high}}} = 10$ (FP16 mantissa). The special case $n = -1$ corresponds to when the 11th mantissa bit is 1 and the remaining bits are 0.

Underflow conditions are met when its exponent falls below the minimum representable exponent for FP16. Specifically:

$$\begin{cases} E_{\text{offset}} - l_{M_{\text{high}}} + b_{\text{low}} - 3 < N & \text{(gradual underflow)} \\ E_{\text{offset}} + b_{\text{low}} - 3 < N & \text{(underflow)} \end{cases} \quad (4)$$

where $b_{\text{low}} = 15$ is the FP16 exponent bias. The probabilities for underflow and gradual underflow are then:

$$\begin{cases} P_{u+gu}(E_{\text{offset}}) = \sum_{N=E_{\text{offset}} - l_{M_{\text{high}}} + b_{\text{low}} - 2}^{l_M - l_{M_{\text{high}}} - 1} (P(N, T) + P(N, R)) \\ P_u(E_{\text{offset}}) = \sum_{N=E_{\text{offset}} + b_{\text{low}} - 2}^{l_M - l_{M_{\text{high}}} - 1} (P(N, T) + P(N, R)) \end{cases} \quad (5)$$

As shown in Fig. 2(a), underflow becomes a significant concern when the offset exponent of the original FP32 number is small. If subnormals are not

supported by the hardware, the probability of gradual underflow exceeds 10% at $E_{\text{offset}} = 0$. Conversely, if subnormals are supported, significant underflow occurs only below $E_{\text{offset}} = -10$, approaching 100% at $E_{\text{offset}} < -12$. This analysis underscores the necessity of careful handling of small-magnitude numbers to preserve precision.

3.1.3. Applicability and Tunable Scaling

In practical scenarios, the exact value of N (number of leading zeros in V_{low}) is not directly known to the user. When underflow begins (e.g., $N = 10$), if the effective exponent of V_{low} (i.e., $(E' - 15 - 12 - 10) < -24$) falls below the minimum FP16 exponent, fewer than 22 bits of precision are preserved. If complete underflow occurs ($N = 0$) and $(E' - 15 - 12 - 0) < -24$, the precision can collapse to merely 11 bits, equivalent to a direct FP32-to-FP16 conversion. To counteract this, scaling the low part (V_{low}) is essential.

Rule 1 (Underflow Mitigation): Under RN rounding, when the absolute value of an FP32 number is below 2^{-2} , the low part must be scaled to preserve 22 bits. If the value is below 2^{-12} , decomposition without sufficient scaling will lead to significant precision loss.

It is important to note that if the original FP32 number is below the FP16 subnormal threshold (2^{-24}), both V_{high} and V_{low} parts require scaling, which is beyond the current scope of this work.

Conversely, amplifying V_{low} introduces the risk of overflow if the scaled value exceeds the representable upper bound of FP16. Let the scaling factor be $sf = 2^{sb}$, where (sb) is the scaling exponent. Overflow may occur when the scaled low part reaches its upper range. Considering the case where $N = 0$, the effective offset exponent of the scaled low part becomes $E' - 15 - 12 + sb$. If this value exceeds the maximum FP16 offset exponent (i.e., 15), additional precision loss may result from overflow. To prevent this, we introduce the following rule:

Rule 2 (Overflow Prevention): Under RN rounding, if large FP32 values are present in the input, the scaling factor should not exceed 2^{12} to avoid overflow in the lower component.

Rules 1 and 2 collectively define the allowable bounds for the scaling exponent sb . As expressed in Eq. 6, these bounds ensure that the decomposition algorithm preserves 22 effective mantissa bits from the original FP32

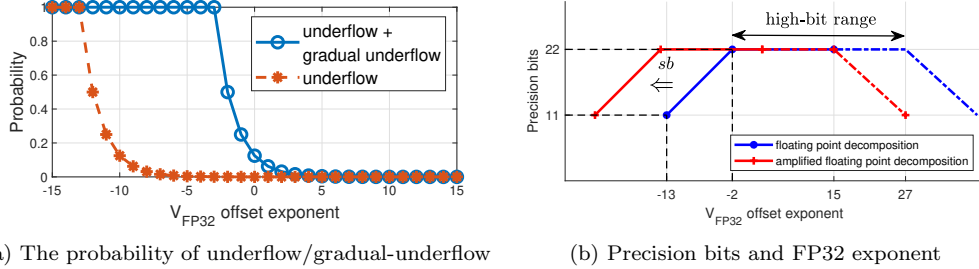


Figure 2: Analysis of FP32 underflow/gradual underflow and precision bits

input. By selecting an appropriate sb within this range, the decomposition maintains near-full precision while avoiding both underflow and overflow.

$$-24 + 22 - (E' - 15)_{\min} \leq sb \leq 15 + 12 - (E' - 15)_{\max} \quad (6)$$

The choice of sb depends on the input data’s dynamic range and required numerical precision. When the input distribution is unknown, a conservative assumption is to treat the values as spanning the entire FP16 representable range, i.e., with offset exponents $(E' - 15)_{\min} = -14$ and $(E' - 15)_{\max} = 15$. Under this assumption, a scaling exponent of $sb = 12$ is a reasonable and robust choice. In many deep learning workloads, where both weights and updates typically have small magnitudes, the upper bound constraint (rule 2) is often less critical. Hence, a scaling factor of 2^{12} remains suitable in practice, effectively shifting the precision curve to cover a wider range of small-magnitude numbers.

Based on Eq. 6, Fig. 2(b) shows how the number of retained mantissa bits varies with the offset exponent of the original FP32 input, both with and without scaling. Without amplification, precision degrades gradually as the exponent decreases, particularly for values approaching the FP16 subnormal range. When applying a scaling exponent of $sb = 12$, the curve is effectively shifted left by 12 bits, significantly expanding the high-precision region. This means input values with offset exponents in the range $([15, 27])$, which cannot be represented in FP16 format, are remapped into the representable range, thereby maximizing bit retention within the FP16 domain and ensuring that the low-order component remains representable and significant.

3.2. Half-to-Single Precision Matrix Multiplication and Error Analysis

Matrix multiplication is a core operation in deep learning and scientific computing. To accelerate computation, modern accelerators frequently em-

ploy low-precision units (e.g., FP16) instead of FP32. However, converting FP32 inputs directly to FP16 reduces precision to 11 bits. To mitigate this, SGEMM-cube employs a half-to-single precision conversion algorithm, as formulated in Eq. 7:

$$\left\{ \begin{array}{l} A_{\text{half}} = \text{to_half}(A_{\text{single}}), \quad R_{A,\text{half}} = \text{to_half}((A_{\text{single}} - \text{to_single}(A_{\text{half}})) \times sf) \\ B_{\text{half}} = \text{to_half}(B_{\text{single}}), \quad R_{B,\text{half}} = \text{to_half}((B_{\text{single}} - \text{to_single}(B_{\text{half}})) \times sf) \\ C_{\text{single}} = A_{\text{single}} B_{\text{single}} \\ \quad \approx (A_{\text{half}} + R_{A,\text{half}}/sf)(B_{\text{half}} + R_{B,\text{half}}/sf) \\ \quad \approx A_{\text{half}} B_{\text{half}} + B_{\text{half}} R_{A,\text{half}}/sf + A_{\text{half}} R_{B,\text{half}}/sf + \cancel{R_{A,\text{half}} R_{B,\text{half}}/sf^2} \end{array} \right. \quad \begin{array}{l} \nearrow 0 \\ (7) \end{array}$$

Here, $A_{\text{single}}, B_{\text{single}}$ are FP32 inputs, and C_{single} is the FP32 output. The high parts $A_{\text{half}}, B_{\text{half}}$ and scaled low parts $R_{A,\text{half}}, R_{B,\text{half}}$ are stored as FP16 values. The final term, $R_{A,\text{half}} R_{B,\text{half}}/sf^2$, is typically negligible due to its significantly smaller magnitude and can be safely omitted without substantial impact on accuracy.

This method inherently introduces errors from several sources: the initial FP32-to-FP16 decomposition, subsequent rounding operations during intermediate computations, and the accumulation of products. The choice of RN rounding is critical as it provides superior precision compared to RZ rounding by minimizing systematic bias. Furthermore, the accumulation of intermediate products in matrix multiplication can introduce both under-flow and cancellation errors. Storing intermediate results in FP32 format (or higher precision) rather than lower-precision types helps prevent precision loss during accumulation. In addition, carefully reordering the accumulation sequence can significantly mitigate rounding error propagation and enhance numerical stability.

3.3. System-Level Optimizations

While the numerical decomposition scheme in Sec. 3 ensures FP32-level accuracy, sustaining high throughput on Ascend NPUs further requires careful system-level optimizations. In particular, the hierarchical memory design of the DaVinci architecture introduces substantial challenges: the bandwidth from main memory to L1 is limited, and naive pipelines leave the FP16 cube units underutilized. To mitigate these bottlenecks, we introduce two complementary strategies: *cache-aware blocking* and *double-buffered pipelining*. The

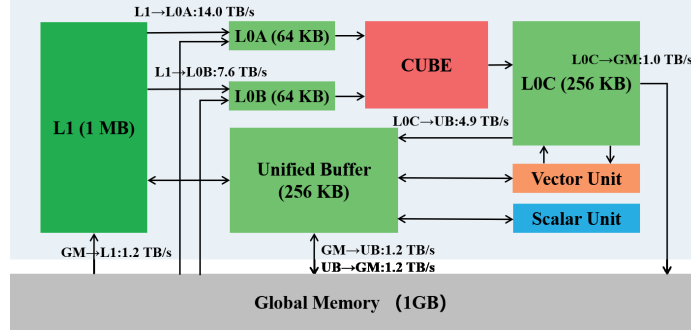


Figure 3: DaVinci architecture of Huawei Ascend NPU AI core

former minimizes memory traffic by maximizing data reuse in L1, while the latter overlaps computation with data transfers to hide latency. Together, these optimizations enable SGEMM-cube to approach the theoretical FP32-equivalent peak throughput.

3.3.1. Cache-Aware Blocking

Efficient utilization of the L1 buffer is critical for sustaining high throughput on Ascend NPUs, where the bandwidth from main memory to L1 is substantially lower than that from L1 to the compute units (Fig. 3). Without careful blocking, frequent L1 refills stall the FP16 cube units, resulting in under-utilization of compute resources.

To address this bottleneck, we develop an *L1-aware blocking strategy* tailored to the hierarchical memory design of Ascend. The design is guided by two principles:

(1) Maximizing L1 Reuse for Matrix A: Blocks of matrix A are designed to reside in L1 for as long as possible, maximizing their reuse across multiple inner-loop iterations.

(2) Enabling Double Buffering for Matrix B: Space is reserved in L1 for double buffering of matrix B blocks, allowing for alternating access and prefetching.

These principles aim to minimize data movement between main memory and L1 while maintaining a steady supply of operands to the cube units. Fig. 4 shows the block layout: A blocks are stored in row-major order in L1, and B blocks are streamed column-wise into alternating L1 buffers.

The degree of reuse is quantified by the number of A blocks that can be

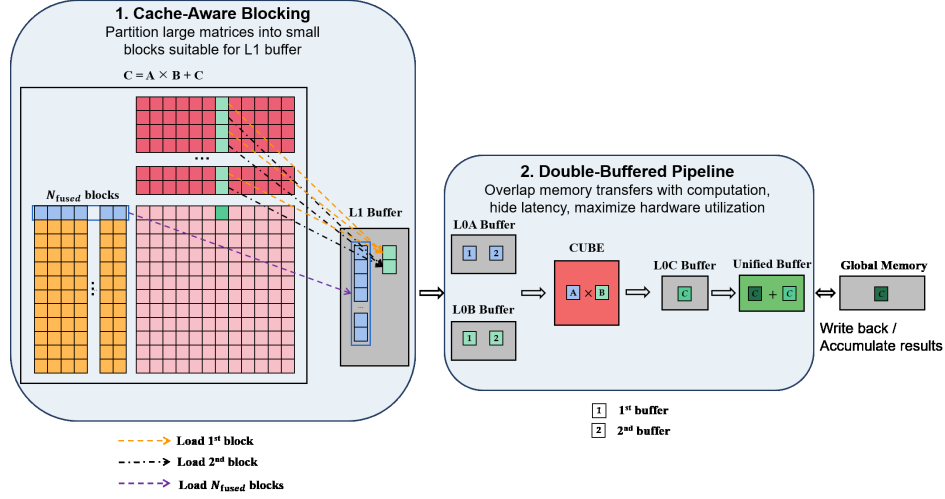


Figure 4: Matrix blocking based on L1 cache reuse

held in L1 simultaneously:

$$N_{\text{fused}} = \text{int} \left(\frac{L1 - 2b_k b_n}{b_m b_k} \right) = \text{int} \left(\frac{L1}{b_m b_k} - 2 \frac{b_n}{b_m} \right) = f \frac{L1}{b_m b_k} \quad (8)$$

where b_m and b_k denote the block height and width of A , and f ($0.92 \leq f \leq 1$ in our experiments) accounts for the correction from $\frac{b_n}{b_m} \sim O(1)$ and the floor operation. A larger N_{fused} implies greater reuse of A and fewer reloads of B from main memory.

The total memory traffic between main memory and L1 for matrices A , B , and C can be expressed as:

$$\left\{ \begin{array}{l} A_r = mk, \\ B_r = \frac{mkn}{N_{\text{core}} b_m}, \\ C_{\text{rw}} = \frac{2mkn b_m}{f L1}, \\ \text{data}_{\text{rw}} = A_r + B_r + C_{\text{rw}}, \end{array} \right. \quad (9)$$

where m, k, n denote the matrix dimensions, b_m, b_k, b_n the block sizes, $N_{\text{core}} = 32$ the number of AI cores, and f the L1 fusion efficiency factor. Here, A_r counts each A block once, B_r reflects the number of reloads of B blocks across

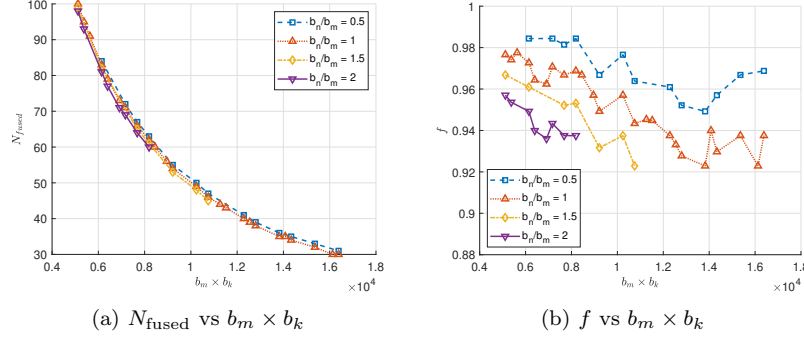


Figure 5: Impact of blocking size on N_{fused} and f

cores, and C_{rw} accounts for reading and writing C through the unified buffer N_{fused} times.

Block sizes are subject to hardware constraints arising from cube computation alignment and buffer capacities:

$$\begin{cases} b_m, b_k, b_n \equiv 0 \pmod{16} & (\text{cube alignment}) \\ b_m \times b_k \leq 64 \times 256 & (\text{L0A capacity}) \\ b_k \times b_n \leq 64 \times 256 & (\text{L0B capacity}) \\ b_m \times b_n \times 6 \leq 248 \times 1024 & (\text{L0C and UB capacity}) \end{cases} \quad (10)$$

Fig. 5 shows how N_{fused} and f vary with $b_m b_k$ and b_n/b_m . In the range $0.5 \leq b_n/b_m \leq 2$, N_{fused} is roughly inversely proportional to $b_m b_k$, with weak dependence on b_n/b_m . The fusion efficiency f remains between 0.92 and 1.0, indicating high L1 utilization. As $b_m b_k$ increases, f decreases slowly, while an increase in b_n/b_m leads to a monotonic decrease in f . Due to the constraints imposed by Eq. 10, larger b_n/b_m values can restrict the number of feasible block configurations.

Exploring the feasible (b_m, b_k, b_n) space under Eq. (10) shows that N_{fused} decreases with $b_m b_k$, while f remains high for $0.5 \leq b_n/b_m \leq 2$ (Fig. 5). Minimizing the estimated memory traffic yields:

$$b_{m,\text{opt}} \approx \sqrt{\frac{f L1}{2 N_{\text{core}}}} \quad (11)$$

which gives $86 < b_{m,\text{opt}} < 90$ for Ascend 910A NPU. Rounding to the nearest multiple of 16 (due to cube alignment) leads to $b_m = 96$, a configuration

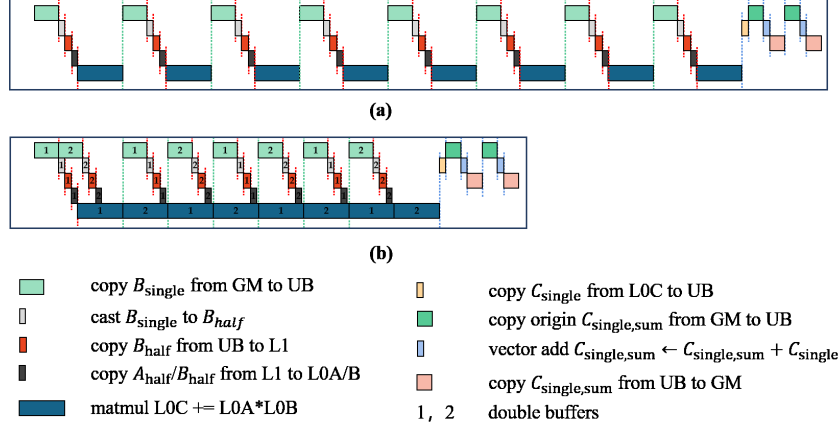


Figure 6: Comparison of single- and double-buffered pipelines based on L1 reuse

that consistently delivers high L1 reuse and serves as the baseline for our performance evaluation in Sec. 4.2.

3.3.2. Double-Buffered Pipelining

While cache-aware blocking reduces memory traffic, the pipeline structure still constrains throughput: in a single-buffered design, each GEMM step must wait for data to be fully loaded into L1 before computation, leaving the cube units idle (Fig. 6 (a)). To overcome this limitation, we implement a double-buffered pipeline that overlaps data movement with computation across L1, L0A, and L0B, thereby maximizing concurrency (Fig. 6 (b)).

The key idea is to maintain two L1 buffers for matrix B blocks: while one buffer feeds the cube unit, the other prefetches the next block from global memory. This ensures that when the current block computation finishes, the next block is already staged in L1. Matrix A blocks, already optimized for reuse, remain resident in L1 across multiple inner-loop iterations, following the cache-aware blocking strategy in Sec. 3.3.1.

Let T_{comp} and T_{mem} denote the computation and transfer time per block. A single-buffered pipeline requires $T_{\text{comp}} + T_{\text{mem}}$ per iteration, whereas the double-buffered design approaches $\max(T_{\text{comp}}, T_{\text{mem}})$, effectively hiding memory latency whenever $T_{\text{comp}} \gtrsim T_{\text{mem}}$.

The decomposition in Eq. 7 produces three structurally similar GEMM terms, each of which can be computed independently. To fully exploit the parallelism of the Ascend architecture and hide memory latency, we implement each term using a double-buffered GEMM pipeline that overlaps data

Algorithm 1: Double-buffered GEMM for one decomposition term in SGEMM-cube

Input: Matrix term (A, B) partitioned into $M \times K$ and $K \times N$ blocks; scaling factor sf
Output: Accumulated result $C \leftarrow A \times B$
foreach *block row of A in parallel over N_{core} cores* **do**
 foreach *group of N_{fused} A -blocks* **do**
 // Stage A blocks into L1 (once per group)
 prefetch and **convert** A blocks to FP16, store in L1;
 foreach *column block of B* **do**
 // Double-buffered prefetch of B blocks
 while *computing on buffer p* **do**
 └ **prefetch** next B block to buffer q ;
 // GEMM computation
 $C_{blk} \leftarrow A_{blk} \times B_{blk} + C_{blk}$;
 // Write-back if UB capacity reached
 accumulate and store C_{blk} to global memory;

transfers with computation. This approach ensures that while one set of matrix blocks is being processed by the FP16 cube units, the next set is prefetched into L1, thereby keeping the compute units busy and minimizing idle cycles. Algorithm 1 outlines the generic procedure for one such term, which is directly applicable to $A_{\text{half}}B_{\text{half}}$, $B_{\text{half}}R_{A,\text{half}}/sf$, and $A_{\text{half}}R_{B,\text{half}}/sf$.

4. Experimental Results

This section evaluates SGEMM-cube along two axes: (i) numerical accuracy of the FP32 emulation (Sec. 4.1), and (ii) sustained throughput and scalability on Ascend NPUs (Sec. 4.2). We compare against FP16 HGEMM and FP32 baselines and report how the proposed system-level optimizations (Sec. 3.3) translate into end-to-end performance gains.

Platforms We use two Ascend platforms and one CPU reference:

- **Ascend 910A:** 192-core 64-bit Kunpeng 920 ARM CPU across 4 sockets (48 cores/socket), organized into 8 NUMA nodes. Each core has 64KB L1, 512KB L2, and 48MB shared L3. The Ascend 910A NPU provides 32 AI cores at 1 GHz with 1.2 TB/s memory bandwidth and *no* native FP32 matrix units. SGEMM-cube and FP16 HGEMM run here. Architectural details are shown in Fig. 3.

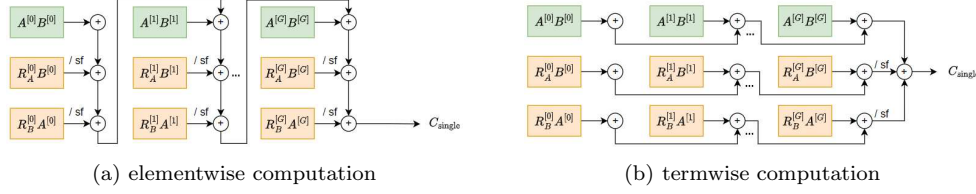


Figure 7: Computation sequences of the SGEMM-cube precision recovery algorithm

- **Ascend 910B3:** 20 AI cores at 1.8 GHz, half the L1 capacity per core relative to 910A, doubled main memory, and 1.6 TB/s bandwidth. Supports native FP32 GEMM with a theoretical peak of 73.73 TFLOPs. We use CANN SGEMM as an FP32 reference.

Baselines and metrics For accuracy, we use FP64 DGEMM as the ground-truth reference and FP32 SGEMM (OpenBLAS) as a software baseline. On NPUs, we compare FP16 HGEMM and SGEMM-cube (elementwise/termwise variants). The relative error is defined in Eq. 12. For performance, we report kernel throughput (TFLOPs) as $\frac{2mkn}{\text{time}}$ on square or rectangular matrices, where $2mkn$ is the total number of floating-point operations and time is the kernel execution time. Unless noted, the termwise accumulation and cache-aware/double-buffered execution are enabled when evaluating SGEMM-cube.

Input generation To probe underflow-prone regimes and cancellation effects, we follow two sampling strategies for FP32 inputs: (a) symmetric ranges $[-2^{\text{offset exponent}}, 2^{\text{offset exponent}}]$ and (b) non-negative ranges $[0, 2^{\text{offset exponent}}]$ (Fig. 8). We evaluate scaling exponents $sb \in \{0, 6, 12\}$ (Sec. 3.1.3).

4.1. Relative Error Evaluation

We first isolate the impact of accumulation order. Fig. 7 (a) shows the *elementwise* approach, which combines the three expansion terms of C_{single} per element and is sensitive to magnitude disparity between $(A_{\text{half}}, B_{\text{half}})$ and $(R_{A,\text{half}}, R_{B,\text{half}})$. Fig. 7 (b) shows the *termwise* strategy that computes each component matrix independently before the final summation, thereby reducing rounding and underflow propagation.

The relative error is

$$\text{err} = \frac{\|C_{\text{true}} - C_{\text{calculated}}\|_2}{\|C_{\text{true}}\|_2}, \quad (12)$$

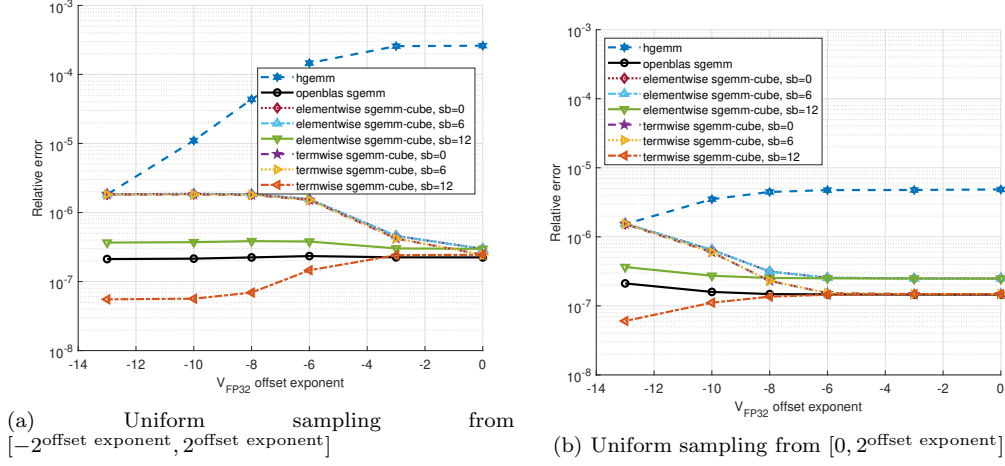


Figure 8: Relative error vs. offset exponent under different input ranges

where C_{true} is obtained via FP64 DGEMM (Kunpeng CPU or 910B3), and $C_{\text{calculated}}$ covers SGEMM-cube (both variants), FP16 HGEMM, and FP32 OpenBLAS SGEMM.

Fig. 8 sweeps the FP32 offset exponent under the two sampling regimes. With symmetric sampling (Fig. 8 (a)), destructive cancellation can depress $\|C_{\text{true}}\|_2$, amplifying the reported relative error (Eq. 12); this effect is absent for non-negative sampling (Fig. 8 (b)). Across both settings, FP16 HGEMM exhibits the highest error ($\sim 10^{-4}$). Without scaling ($sb = 0$), elementwise and termwise SGEMM-cube behave similarly, with termwise slightly better near zero offset exponent, but both trail FP32 SGEMM, highlighting the necessity of residual amplification. Setting $sb = 12$ improves accuracy by 1–2 orders of magnitude, especially in low-exponent regimes prone to underflow; $sb = 6$ is insufficient, validating the analysis in Sec. 3.1.3.

Once scaling is applied, the distinction between accumulation strategies becomes evident. With $sb = 12$, elementwise SGEMM-cube achieves accuracy comparable to baseline SGEMM, whereas termwise SGEMM-cube surpasses it in small-exponent regions. This advantage arises because termwise accumulation prioritizes summing lower-magnitude contributions before larger ones, thereby suppressing rounding errors and enhancing numerical stability. These findings demonstrate that SGEMM-cube, particularly under the termwise scheme, not only matches but can exceed the robustness of native FP32 implementations in challenging numerical regimes.

Fig. 9 examines how error scales with matrix size at offset exponent = 0.

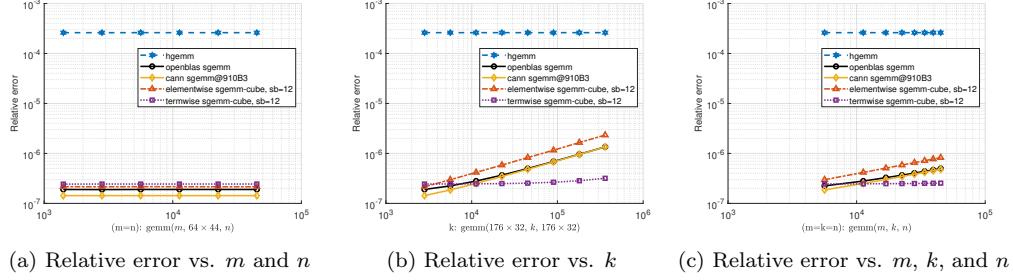


Figure 9: Relative error vs. input matrix sizes

Varying m and n with fixed $k = 64 \times 44$ (Fig. 9 (a)) leaves the error nearly unchanged since accumulation depth is governed by k . Increasing k (Fig. 9 (b) and (c)) stresses summation stability; here, *termwise* SGEMM-cube consistently outperforms FP32 OpenBLAS SGEMM and the elementwise variant, aligning with our design that sums smaller-magnitude contributions first.

4.2. Performance Evaluation

We next quantify how cache-aware blocking and double-buffered pipelining translate to throughput on 910A. Fig. 10 sweeps block sizes and contrasts pipeline designs. The single-buffered pipeline peaks at 41.7 TFLOPs (Fig. 10 (a)). Enabling double buffering raises the peak to 65.3 TFLOPs (Fig. 10 (b)), a **57%** gain by overlapping memory movement with compute and reducing contention. This corresponds to **77%** of the FP32-equivalent theoretical peak on 910A ($256 \text{ TFLOPs}/3 = 85.3 \text{ TFLOPs}$). Low-performing points at small blocks are explained by poor L0A/L0B utilization, which is not explicitly constrained by Eq. 10. The best configuration $(b_m, b_k, b_n, N_{\text{fused}}) = (176, 64, 176, 44)$ achieves its maximum throughput.

Fig. 11 studies size scaling. Increasing m, n boosts throughput past 60 TFLOPs (Fig. 11 (a)), slightly surpassing CANN FP32 SGEMM on 910B3 despite 910A lacking FP32 matrix units. As k increases (Fig. 11 (b)), both SGEMM-cube@910A and CANN FP32@910B3 remain stable; SGEMM-cube reaches 60 TFLOPs versus ~ 63 TFLOPs on 910B3. When jointly scaling m, k, n (Fig. 11 (c)), CANN FP32@910B3 degrades at very large sizes, while SGEMM-cube@910A maintains stable performance and eventually surpasses it, evidence that our L1-aware blocking and double-buffered design sustain utilization even when problem sizes outgrow typical cache capacities.

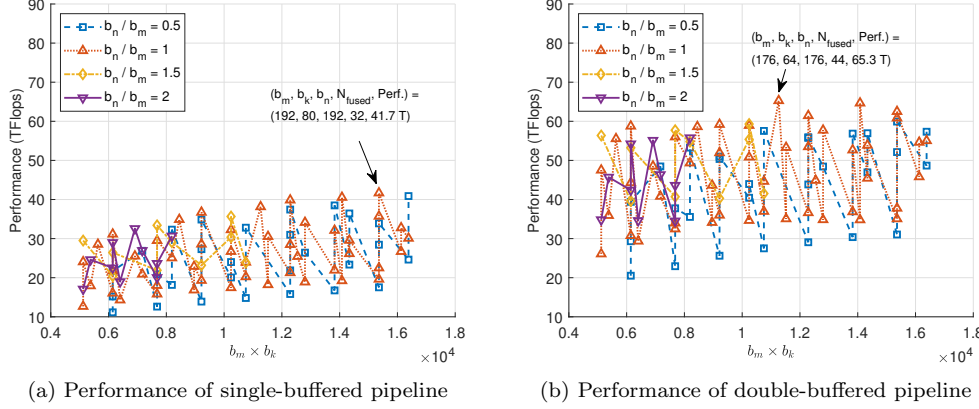


Figure 10: Performance impact of matrix blocking with L1 reuse

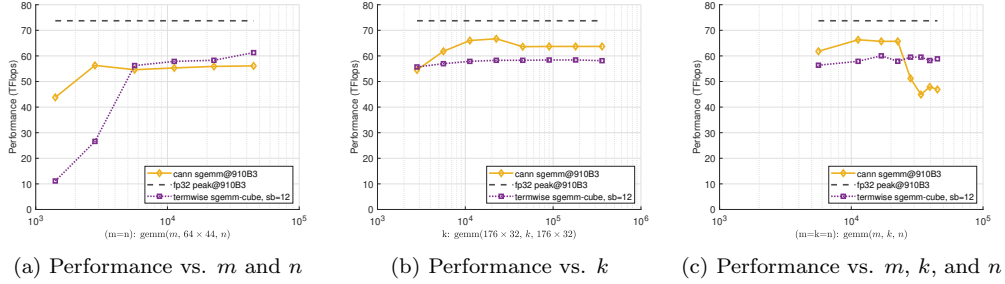


Figure 11: Performance vs. input matrix sizes

5. Conclusions

SGEMM-cube is presented as a high-performance algorithm for emulating FP32 GEMM on low-precision AI accelerators equipped only with FP16 compute units. By combining a decomposition-based FP32-to-FP16 mapping, tunable residual scaling, and term-wise accumulation within a cache-aware double-buffered pipeline, the method achieves both high numerical accuracy and efficient hardware utilization. Empirical evaluation on the Ascend 910A NPU shows that SGEMM-cube preserves up to 22 mantissa bits, demonstrates superior stability in low-exponent regimes, and attains up to 77% of FP32-equivalent peak throughput. In addition, termwise accumulation consistently outperforms elementwise strategies, highlighting the importance of accumulation order in maintaining accuracy. These results indicate that SGEMM-cube is suitable for numerically sensitive workloads on emerging low-precision platforms. Future directions include extending the approach to

lower-precision formats, exploring dynamic scaling strategies, and deploying the method across heterogeneous architectures.

References

- [1] H. Yu, H. Li, H. Shi, T. S. Huang, G. Hua, Any-precision deep neural networks, in: Proceedings of the AAAI Conference on Artificial Intelligence, Vol. 35, 2021, pp. 10763–10771.
- [2] B. Zhuang, L. Liu, M. Tan, C. Shen, I. Reid, Training quantized neural networks with a full-precision auxiliary module, in: Proceedings of the IEEE/CVF conference on computer vision and pattern recognition, 2020, pp. 1488–1497.
- [3] A. Vansteenkiste, J. Leliaert, M. Dvornik, M. Helsen, F. Garcia-Sanchez, B. Van Waeyenberge, The design and verification of mumax3, AIP advances 4 (10) (2014).
- [4] G. P. Müller, M. Hoffmann, C. Dißelkamp, D. Schürhoff, S. Mavros, M. Sallermann, N. S. Kiselev, H. Jónsson, S. Blügel, Spirit: Multifunctional framework for atomistic spin simulations, Physical review b 99 (22) (2019) 224414.
- [5] B. D. Wozniak, F. D. Witherden, F. P. Russell, P. E. Vincent, P. H. Kelly, Gimmik—generating bespoke matrix multiplication kernels for accelerators: Application to high-order computational fluid dynamics, Computer Physics Communications 202 (2016) 12–22.
- [6] M. Cawkwell, E. Sanville, S. Mniszewski, A. M. Niklasson, Computing the density matrix in electronic structure theory on graphics processing units, Journal of chemical theory and computation 8 (11) (2012) 4094–4101.
- [7] P. Micikevicius, S. Narang, J. Alben, G. Diamos, E. Elsen, D. Garcia, B. Ginsburg, M. Houston, O. Kuchaiev, G. Venkatesh, et al., Mixed precision training, arXiv preprint arXiv:1710.03740 (2017).
- [8] M. Rakka, M. E. Fouda, P. Khargonekar, F. Kurdahi, Mixed-precision neural networks: A survey, arXiv preprint arXiv:2208.06064 (2022).

- [9] A. Haidar, S. Tomov, J. Dongarra, N. J. Higham, Harnessing gpu tensor cores for fast fp16 arithmetic to speed up mixed-precision iterative refinement solvers, in: SC18: International Conference for High Performance Computing, Networking, Storage and Analysis, IEEE, 2018, pp. 603–613.
- [10] N. J. Higham, T. Mary, Mixed precision algorithms in numerical linear algebra, *Acta Numerica* 31 (2022) 347–414.
- [11] H. Liao, J. Tu, J. Xia, H. Liu, X. Zhou, H. Yuan, Y. Hu, Ascend: a scalable and unified architecture for ubiquitous deep neural network computing: Industry track paper, in: 2021 IEEE International Symposium on High-Performance Computer Architecture (HPCA), IEEE, 2021, pp. 789–801.
- [12] K. Ozaki, T. Ogita, S. Oishi, S. M. Rump, Error-free transformations of matrix multiplication by using fast routines of matrix multiplication and its applications, *Numerical Algorithms* 59 (2012) 95–118.
- [13] S. Markidis, S. W. Der Chien, E. Laure, I. B. Peng, J. S. Vetter, Nvidia tensor core programmability, performance & precision, in: 2018 IEEE international parallel and distributed processing symposium workshops (IPDPSW), IEEE, 2018, pp. 522–531.
- [14] B. Feng, Y. Wang, G. Chen, W. Zhang, Y. Xie, Y. Ding, Egemm-tc: accelerating scientific computing on tensor cores with extended precision, in: Proceedings of the 26th ACM SIGPLAN symposium on principles and practice of parallel programming, 2021, pp. 278–291.
- [15] H. Ootomo, R. Yokota, Recovering single precision accuracy from tensor cores while surpassing the fp32 theoretical peak performance, *The International Journal of High Performance Computing Applications* 36 (4) (2022) 475–491.
- [16] M. Fasi, N. J. Higham, M. Mikaitis, S. Pranesh, Numerical behavior of nvidia tensor cores, *PeerJ Computer Science* 7 (2021) e330.
- [17] Z. Ma, H. Wang, G. Feng, C. Zhang, L. Xie, J. He, S. Chen, J. Zhai, Efficiently emulating high-bitwidth computation with low-bitwidth hardware, in: Proceedings of the 36th ACM International Conference on Supercomputing, 2022, pp. 1–12.

- [18] G. Li, J. Xue, L. Liu, X. Wang, X. Ma, X. Dong, J. Li, X. Feng, Unleashing the low-precision computation potential of tensor cores on gpus, in: 2021 IEEE/ACM International Symposium on Code Generation and Optimization (CGO), IEEE, 2021, pp. 90–102.
- [19] W. Kahan, Ieee standard 754 for binary floating-point arithmetic, Lecture Notes on the Status of IEEE 754 (94720-1776) (1996) 11.